

## Overview of Recent Alcator C-Mod Research

E.S. Marmor 1), B. Bai 1), R.L. Boivin 4), P.T. Bonoli 1), C. Boswell 1), R. Bravenec 3), B. Carreras 5), D. Ernst 1), C. Fiore 1), S. Gangadhara 1), K. Gentle 3), J. Goetz 6), R. Granetz 1), M. Greenwald 1), K. Hallatschek 7), J. Hastie 15), J. Hosea 2), A. Hubbard 1), J.W. Hughes 1), I. Hutchinson 1), Y. In 12), J. Irby 1), T. Jennings 1), D. Kopon 16) G. Kramer 2), B. LaBombard 1), W.D. Lee 1), Y. Lin 1), B. Lipschultz 1), J. Liptac 1), A.Lynn 3), K. Marr 1), R. Maqueda 8), E. Melby 9), D. Mikkelsen 2), D. Mossessian 1), R. Nazikian 2), W.M. Nevins 13), R. Parker 1), T.S. Pedersen 10), C.K. Phillips 2), P. Phillips 3), C.S. Pitcher 11), M. Porkolab 1), J. Ramos 1), M. Redi 2), J. Rice 1), B.N. Rogers 14), W.L. Rowan 3), M. Sampsell 3), G. Schilling 2), S. Scott 2), J. Snipes 1), P. Snyder 4), D. Stotler 2), G. Taylor 2), J.L. Terry 1), H. Wilson 15), J.R. Wilson 2), S.M. Wolfe 1), S. Wukitch 1), X.Q. Xu 13), B. Youngblood 1), H. Yuh 1), K. Zhurovich 1), S. Zweben 2)

1) Massachusetts Institute of Technology, Cambridge, MA USA

2) Princeton Plasma Physics Laboratory, Princeton, NJ USA

3) University Texas, Austin, TX USA

4) General Atomics, San Diego, CA USA

5) Oak Ridge National Laboratory, Oak Ridge, TN USA

6) University of Wisconsin, Madison, WI USA

7) Max Planck Institute of Plasma Physics, Garching, Germany

8) Los Alamos National Laboratory, Los Alamos, NM USA

9) CRPP, Lausanne, Switzerland

10) Columbia University, New York, NY USA

11) Institute for Aerospace Studies, University of Toronto, Toronto, Ontario, Canada

12) University of Idaho, Moscow, ID, USA

13) Lawrence Livermore National Laboratory, Livermore, CA USA

14) Dartmouth University, Hanover NH USA

15) EURATOM/UKAEA Fusion Association, Culham Science Centre, Abingdon, Oxon, UK

16) Cornell University, Ithaca, NY, USA

e-mail contact for main author: [marmor@psfc.mit.edu](mailto:marmor@psfc.mit.edu)

**Abstract.** Research on the Alcator C-Mod tokamak [1] is focused on high particle- and power-density plasma regimes to understand particle and energy transport in the core, the dynamics of the H-mode pedestal, and scrape-off layer and divertor physics. The auxiliary heating is provided exclusively by RF waves, and both the physics and technology of RF heating and current drive are studied. The momentum which is manifested in strong toroidal rotation, in the absence of direct momentum input, has been shown to be transported in from the edge of the plasma following the L to H transition, with time scale comparable to that for energy transport. In discharges which develop internal transport barriers (ITBs), the rotation slows first inside the barrier region, and then subsequently outside of the barrier foot. Heat pulse propagation studies using sawteeth indicate a very narrow region of strongly reduced energy transport, located near  $r/a = 0.5$ . Addition of on-axis ICRF heating arrests the buildup of density and impurities, leading to quasi-steady conditions. The quasi-coherent mode associated with EDA H-mode appears to be due to a resistive ballooning instability. As the pedestal pressure gradient and temperature are increased in EDA H-mode, small ELMs appear; detailed modeling indicates that these are due to intermediate  $n$  peeling-ballooning modes. Phase Contrast Imaging (PCI) has been used to directly detect density fluctuations driven by ICRF waves in the core of the plasma, and mode conversion to an intermediate wavelength Ion Cyclotron Wave has been observed for the first time. The bursty turbulent density fluctuations, observed to drive rapid cross-field particle transport in the edge plasma, appear to play a key role in the dynamics of the density limit. Preparations for quasi-steady-state Advanced Tokamak studies with lower hybrid current drive are well underway, and time dependent modeling indicates that regimes with high bootstrap fraction can be produced.

## 1. Transport Barriers and Plasma Rotation

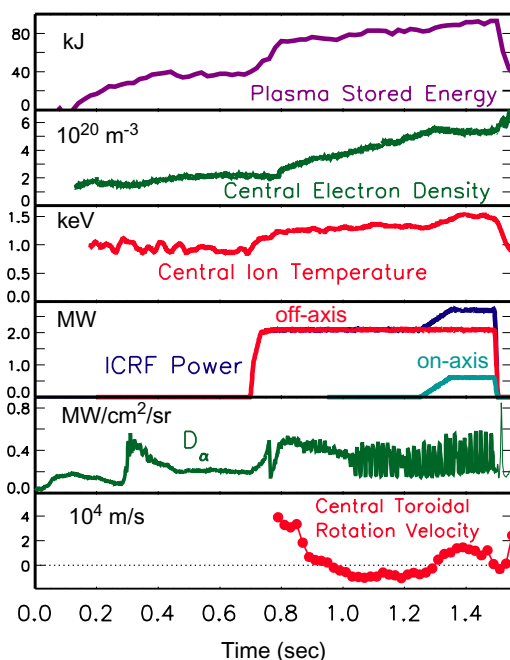


FIG. 1. Time histories of plasma parameters for an off-axis ITB discharge. Once the ITB has formed, on-axis heating arrests the density and impurity buildup.

the half minor radius, on either the low field or the high field side, triggers a transport barrier, which is localized also at about  $r/a=0.5$ . Following the transition, the central density rises monotonically, and the density profile becomes strongly peaked, in spite of the fact that there is no core particle source. This phenomenon is reproducibly observed whenever the plasma enters EDA H-mode[2] following the application of the off-axis heating. Coincident with the transition, the co-current toroidal rotation, which is normally seen in high pressure C-Mod discharges, is strongly reduced and even reverses direction. Figure 1 shows the time histories of plasma parameters for a typical discharge. The off-axis heating (shown in red) is applied starting at 0.7 seconds. In this case, the central toroidal field was 4.45 Tesla, putting the hydrogen minority cyclotron resonance for the 80 MHz waves at  $r/a=0.55$  to the high field side of the magnetic axis. Adding power at a second ICRF frequency (70 MHz, shown in green), to heat near the plasma axis, can arrest the density peaking, while maintaining the transport barrier, leading to a quasi-steady state which has been maintained for up to 15 energy confinement times. Transport modeling[3, 4], using the TRANSP code, reveals that the total effective energy and particle transport are reduced inside the barrier region by about a factor of 10 during the off-axis only phase; once the on-axis power is added, and the density and impurity build-up is arrested, the transport increases, but remains more than a factor of 2 lower than it was before the ITB formation. Unlike most ITB discharges, these do not require current ramps and are produced in a normal shear configuration; the plasmas continue to sawtooth throughout. Besides the interesting implications of maintaining  $q < 1$  on axis, this has presented the opportunity to use the sawteeth for transient probing of the electron energy transport. Figure 2 shows the results of such an analysis[3], where the time after the sawtooth crash for the x-ray emissivity to peak is plotted as a function of radius (red squares). There is a clear energy transport barrier, located just outside the half-radius for this 0.21m minor radius plasma. A simple model for the heat-pulse  $\chi$  profile, with a nearly singular dip at the

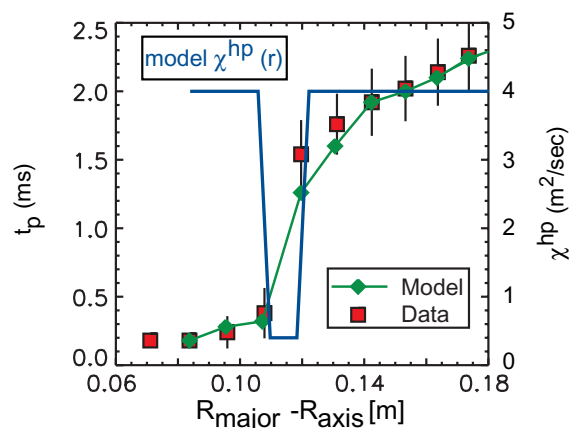


FIG. 2. Sawtooth heat-pulse propagation.  $t_p$  is the time to peak in the x-ray signal following the sawtooth crash. The model results use the  $\chi$  profile shown in blue.

A series of experiments has been carried out to investigate the triggering and control of internal transport barriers, using multiple frequency ICRF tools. We find that placing the minority resonance at approximately the

location of the barrier foot, gives excellent agreement with the experimental data, as shown by the green curve. The transient analysis also indicates that this region of sharply reduced transport moves quickly inward in minor radius from the outer regions of the plasma to the final location near the half radius.

While these barriers are most reliably triggered using off-axis ICRF heating, they also occur in ohmic EDA-H-modes[5]. In the ohmic cases, the time scale to develop the ITB is longer (typically  $\sim 10$  energy confinement times), but the subsequent dynamics are very similar to those of the ICRF-triggered barrier discharges. The application of on-axis ICRF heating in the ohmic ITB cases also arrests the density and impurity build-up, leading to quasi-steady conditions.

Neither the ICRF nor ohmic ITB discharges have explicit external applied momentum sources; nevertheless, rotation plays a central role in the dynamics of these discharges. Coincident with the transition, the core co-current toroidal rotation, which is normally seen in high pressure C-Mod discharges[6,7], is reduced, or even changes direction. Recent modifications to the high resolution x-ray arrays used to measure the rotation allow us to diagnose the temporal evolution of the radial profiles, and thus to examine the momentum transport. Figure 3 shows the time evolution of plasma rotation at three different radial locations ( $\rho \equiv r/a = 0, 0.3, 0.6$ ). Figure 4 shows the radial profiles of plasma density at 3 times

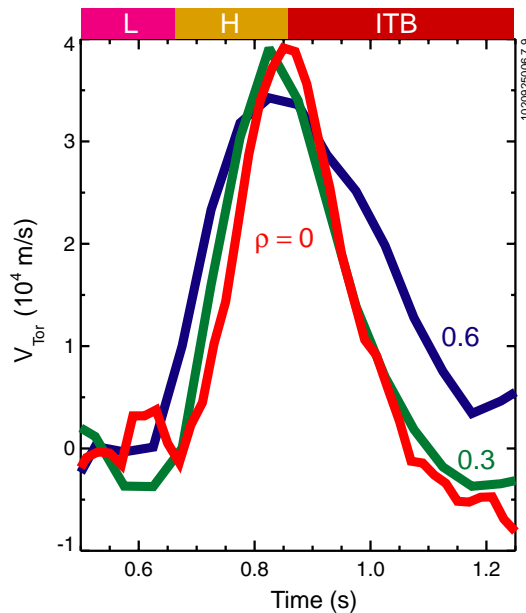


FIG. 3. Time histories of the toroidal rotation velocity at 3 radial locations: near the magnetic axis ( $\rho = 0$ ); off-axis but inside the foot of the barrier ( $\rho = 0.3$ ); and just outside the barrier ( $\rho = 0.6$ ).

large minor radius, as momentum is transported in from the edge. While detailed modeling is not yet complete, the characteristic time scale indicates that  $\chi_\phi$  is comparable to  $\chi_i$ . As the internal barrier begins to form, around 0.9 seconds, it is the core rotation which decreases first; there is a significant delay before the rotation drops outside of the barrier.

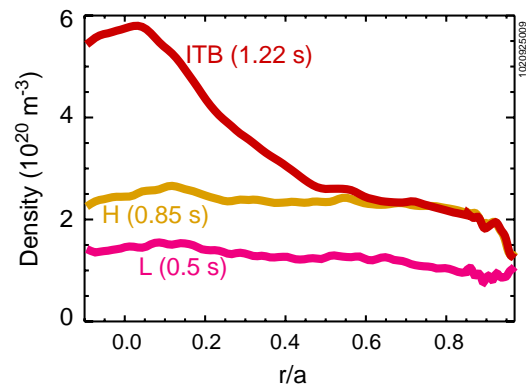


FIG. 4. Radial profiles of plasma density at 3 times during the development of an ITB. The transition from L to H occurs at 0.68 seconds; the density profile begins to peak at 0.9 seconds. The foot of the ITB is located at  $r/a \approx 0.5$

during the same discharge. Several interesting features can be seen in the rotation data. At the L to H transition ( $t = 0.68$ s), the plasma begins to rotate first at

## 2. H-Mode Pedestal Stability

The baseline operating regime for proposed burning plasma experiments is an ELMy H-mode. Standard H-mode operation for most tokamaks includes large type I ELMs, which can cause unacceptably high peak heat loads on the first wall. There is a need to identify and characterize regimes without large ELMs but which do have good H-Mode confinement. On C-Mod, such regimes have been achieved with the Enhanced D-Alpha (EDA) and type II ELMy discharges.

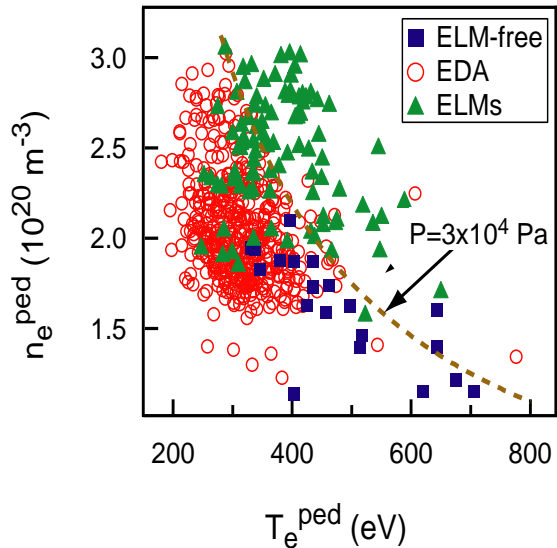


FIG. 5. Plot showing the regions of pedestal  $n_e$  and  $T_e$  with ELM-free, EDA and ELMy H-modes.

Detailed explorations of H-Mode pedestal dynamics and ELM/EDA relaxation mechanisms, utilizing the very high spatial resolution diagnostics available on C-Mod, have revealed a number of interesting new phenomena. The quasi-coherent mode (QCM)[8], which appears to be responsible for enhanced particle transport across the edge barrier in EDA H-modes[9], has a clear magnetic component; the  $k$  spectrum of the QCM has been measured ( $k_R \approx 5 cm^{-1}$ ) with phase contrast imaging [10] as well as with probes. Comparisons of the experiments with MHD stability calculations, in particular the BOUT code [11] are consistent with the hypothesis that the QCM is due to a

resistive ballooning instability, in particular, the resistive x-point mode [10].

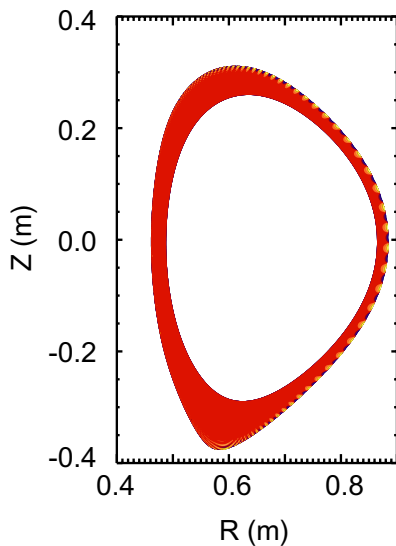


FIG.6. Spatial distribution of displacements for  $n=30$  peeling-ballooning instability. Plasma conditions correspond to ELMy H-Mode.

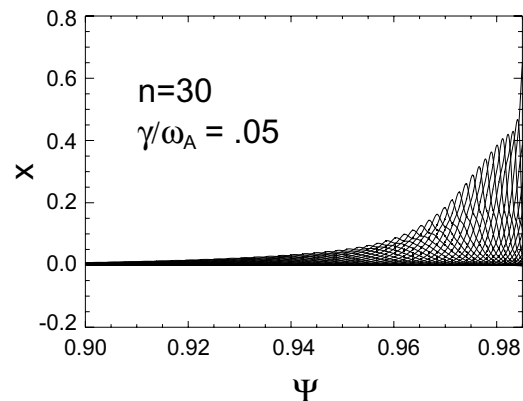


FIG. 7. Profiles of  $n=30$  eigenfunctions for poloidal harmonics.  $X$  is the relative displacement, and  $\Psi$  is normalized flux.

As the pressure and pressure gradient at the H-mode barrier are increased, a regime with small high-frequency ELMs

develops, and the QCM either disappears, or is masked by the ELM activity. In these higher pressure H-modes, the small ELMs regulate the edge pressure and prevent impurity accumulation. Figure 5 illustrates that the ELM regime generally occurs at increased edge barrier pressure gradient and higher pedestal temperature; both pressure drive and collisionality could be playing important roles.

Infinite- $n$  ideal ballooning stability of the C-Mod plasma edge has been analyzed [12] using the BALOO code[13]. When the effects of the expected edge bootstrap current are included, all discharges studied are found to be high- $n$  ballooning stable. Intermediate- $n$  ( $5 < n < 60$ ) stability has been assessed using the ELITE[14, 15] and KINX[16] codes. For conditions typical of the small ELM regime, peeling-ballooning modes with  $n > 20$  are found to be unstable. Lower  $n$ -modes are stable, consistent with the lack of type I ELMs in C-Mod; type I ELMs have been attributed to  $n < 10$  on, for example, DIII-D[17]. The spatial distribution of displacements for a typical case ( $n=30$ ) using ELITE is shown in figure 6. The corresponding radial eigenfunctions for the poloidal harmonics used in the Fourier expansion are shown in figure 7. These modes are stable for the conditions typical of the EDA H-mode, and are believed to be responsible for the ELM activity which is observed in the higher edge pressure cases.

### 3. Ion Cyclotron RF Mode Conversion

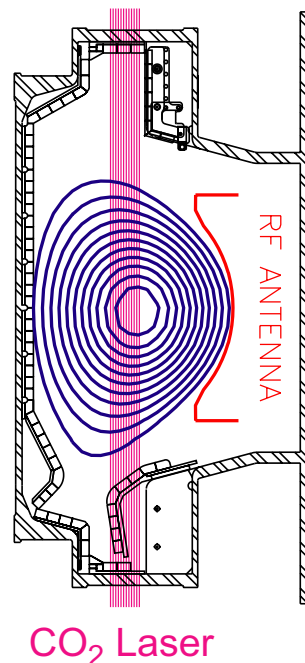


FIG 8. Experimental setup for the PCI diagnostic. The detector has 12 channels, and the beam can be moved to cover a different segment of maior radius.

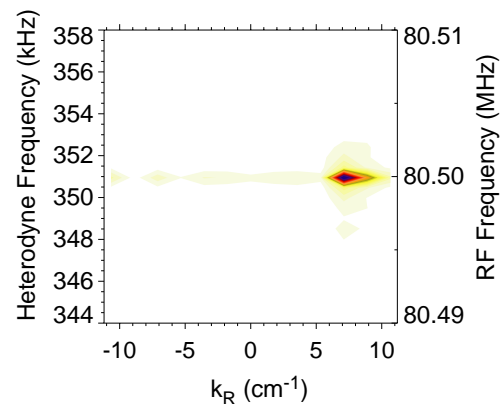


FIG. 9. Frequency-wavenumber spectrum showing the ICW mode converted wave at  $k_R \approx 8 \text{ cm}^{-1}$ .

Auxiliary heating on C-Mod is currently accomplished with ICRF (source powers of 4 MW near 80 MHz fixed, plus 4 MW at 40 MHz to 80 MHz tunable). Routine heating is done with H or  $^3\text{He}$  minority scenarios (5.4 Tesla and 8 Tesla respectively at 80 MHz)[18]. Mode

conversion techniques hold promise for current and especially flow drive[19]. Detailed experiments have been done to study the mode conversion process[20], using the Phase Contrast Imaging (PCI) diagnostic to measure directly the density fluctuations in the plasma which are driven at the RF frequency. The diagnostic geometry is shown in Figure 8. The system is sensitive to waves with  $k$  in the radial direction ( $0.4 < k_R < 10 \text{ cm}^{-1}$ ) over the

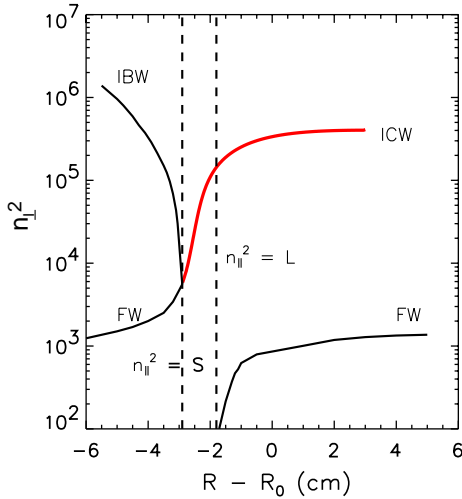


FIG. 10. Dispersion relations for the fast wave (FW), ion cyclotron wave (ICW), and ion Bernstein wave (IBW). The fast wave propagates in from large  $R$  toward the left. The Bernstein and IC waves are born at the mode conversion layer ( $n_{||}^2 = S$ ) and propagate in opposite directions. The FW cutoff ( $n_{||}^2 = L$ ) is also shown.

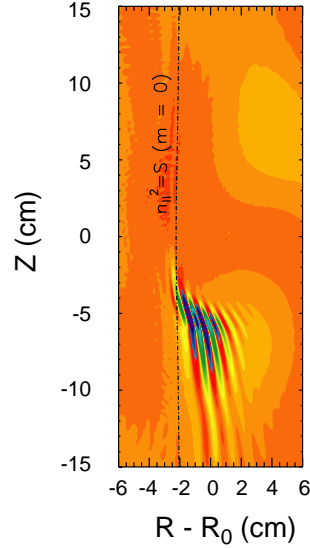


FIG 11. Contours of density fluctuation amplitude at the RF frequency near the core of the plasma for toroidal mode  $n_\phi = 13$ , using data from the TORIC full wave code simulation.

frequency range  $2 < f < 500$  kHz. The laser is modulated at a frequency which is offset by  $\sim 0.3$  MHz from the RF frequency and the waves are detected at the difference frequency. Figure 9 shows the frequency-wavenumber spectrum for a particular mode conversion case. The plasma ion mix was 50% H, 8%  $^3\text{He}$  and 34% D; other parameters were  $B_\phi = 5.8$  T,  $I_p = 1$  MA,  $n_e = 2.5 \times 10^{20} \text{ m}^{-3}$ ,  $T_e = 1.3$  keV. For these conditions, the mode conversion (MC) layer is expected to be far to the high-field side of the region viewed by the PCI. Furthermore, as illustrated in Fig. 10, the IBW should propagate away from the MC layer toward the high field side, out of view of the diagnostic. The observed wave has been identified as an Ion Cyclotron Wave (ICW) of intermediate wavelength, whose existence was predicted by Perkins[21]. The IBW should have a wavelength of about 3 mm, while the ICW is expected to be around 1 cm, in agreement with the measurements[22]. Figure 11 shows a simulation of the conversion process to the ICW using the TORIC 2D full-wave code[23], and the measured wavenumbers and spatial amplitude distribution in the mode conversion region are in good agreement with the TORIC simulations. These results are important, because similar phenomena may be expected in a D-T plasma, and may have impact on proposed heating, current drive and flow shear generation both in present day experiments and in future alpha-particle heated burning plasmas.

#### 4. Edge Transport and Fluctuations

Cross-field transport in the scrape-off layer (SOL) just outside the separatrix has been shown with a number of measurements to be very rapid in Alcator C-Mod; under most conditions, the transport of particles across field lines dominates over the parallel flow of plasma into the divertor, with very important implications for our understanding of SOL processes in general, and particle recycling and ash removal in particular.

Recently, an ultra-high speed CCD camera has been used to image the “bursty” turbulence that is responsible for much of the transport in the SOL, with time resolution down to  $2 \mu\text{s}$ . Individual density structures are seen to grow, move and then disappear on time scales of a few tens of  $\mu\text{s}$ . The structures have typical spatial scales of order 1 cm in the radial and poloidal direction, and are very long in the direction of local  $\mathbf{B}$ . Fluid turbulence models are beginning to give detailed predictions of the nature of the edge fluctuations, and comparisons with the experimental data are in progress[24].

Another important aspect of our edge turbulence experiments are observations that, as the empirical tokamak density limit[25] is approached, the 'bursty' turbulence that is normally restricted to regions far from the separatrix begins to cross the separatrix, leading to a dramatic reduction of global particle confinement and an increase in convective heat losses through the separatrix. This effect is seen both with probe measurements, and directly with the ultra-high speed imaging. Figure 12 shows the relationships obtained from edge probe measurements[26] between effective cross-field particle convection ( $V_{\text{eff}}$ ), edge plasma parallel collisionality ( $\lambda_{ei}/L$ ), and plasma density normalized to the empirical limit,  $n_G$ . As the density increases, an ordered progression occurs: the plasma in the scrape-off layer (SOL) becomes more collisional and the cross-field particle (and heat) convection increases monotonically. Figure 13 shows a single  $2\mu\text{s}$  frame of  $D_\alpha$  emission. For the highest density cases, it is clear from both probe measurements and imaging that the bursty nature of the fluctuations has crossed the separatrix and is present in the closed field-line region of the plasma. In this regime, the edge plasma is apparently dominated by rapid cross-field transport, so that the change in magnetic topology between open and closed field lines no longer has a visible impact on the profiles. The bursty fluctuations carry a convective power loss that affects the power balance of the discharge, suggesting that a key underlying ingredient in the empirical density limit is the physics of cross-field particle transport in the edge and SOL regions.

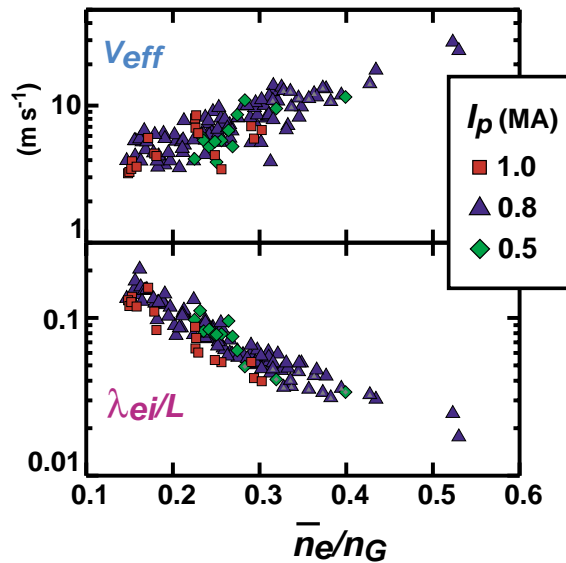


FIG. 12. Effective cross-field convection velocity and parallel collisionality as functions of the normalized plasma density.

fast photodiodes. Experimentally we find that the normalized intensity fluctuation,  $I_{\text{RMS}}/\langle I \rangle$ , as observed with a radial array of views just in front of an inboard midplane gas puff, is

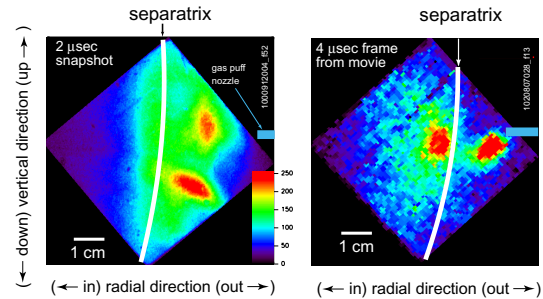


FIG. 13. Ultra-fast images of edge density “blobs”. On the left, with  $n/n_G=0.4$ , the blobs are found only in the SOL. For the higher normalized density case on the right ( $n/n_G=0.7$ ), the bursty transport region has penetrated across the separatrix into the closed field line region. The color table legend shows relative image intensities.

In a related set of experiments, fluctuations in the  $D_\alpha$  emission from localized gas puffs have been measured with imaging arrays of

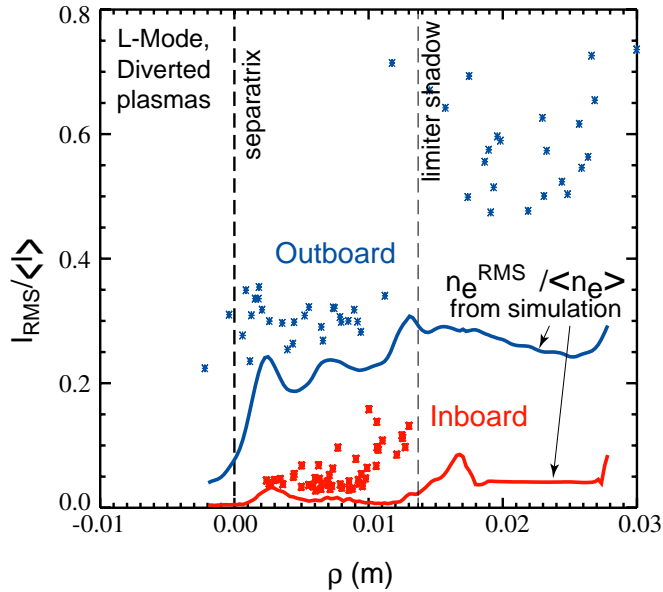


FIG 14. Comparisons of  $D_{\alpha}$  fluctuation profiles across the inner- and outer-midplane scrape-off layers.  $\rho$  is the position of the flux surface, mapped to the outboard midplane. The solid curves are density fluctuation levels from the numerical simulation.

normalized density fluctuation level on the inboard side is much reduced compared to the outboard side (also shown in the figure), and is qualitatively consistent with the observations. However a true quantitative comparison for the inboard side awaits use of measured inboard profiles in the simulation.

Comparisons of particle transport and fueling in single and double null configurations are of direct interest to our program, where the planning for the addition of cryo-pumping for particle control is being completed. There is also considerable debate about the relative merits of single vs. double null for the design of future burning plasma experiments. In a set of experiments to investigate scrape-off layer particle dynamics, we have scanned the magnetic configuration continuously during individual discharges, from lower single null, through double null, to upper single null. Figure 15 shows the results of one such experiment, where imaging in  $D_{\alpha}$  light near the midplane on the high field side of the plasma shows that the ionization of incoming neutrals occurs predominantly at the secondary separatrix, which is significantly outside of the last closed flux surface for single null cases when the primary and secondary separatrices are well separated. The predictions of a simple 1D space, 2D velocity simulation, including the relevant atomic physics[27] are shown for comparison (green curve) and the agreement with the experimental observations is very good. These results follow from the fact that, for low and moderate densities ( $n < 0.5 n_G$ ), the high-field side SOL density profile is relatively flat between the last closed surface and the secondary separatrix, and then falls rapidly beyond that radius. As a consequence, there is strong ionization when incoming neutrals reach the secondary separatrix. One practical implication of these results is the fact that fueling by gas puffing from the inner wall is much more efficient for near double-null discharges.

approximately a factor of ten smaller than that measured on the same flux surface at the outboard midplane. This is shown in figure 14. Inboard and outboard probe measurements of normalized ion saturation current yield similar results. These experimental observations are compared with numerical simulations of edge turbulence, where the electromagnetic turbulence in a 3-D geometry is computed using non-linear plasma fluid equations ( $\lambda_{ei}/L \ll 1$ ). The simulation uses time-averaged profiles measured in the outboard SOL, but computes both the outboard and inboard SOL fluctuations. Since the resistive ballooning mode is the dominant linear instability on the outboard side in the simulations, the predicted



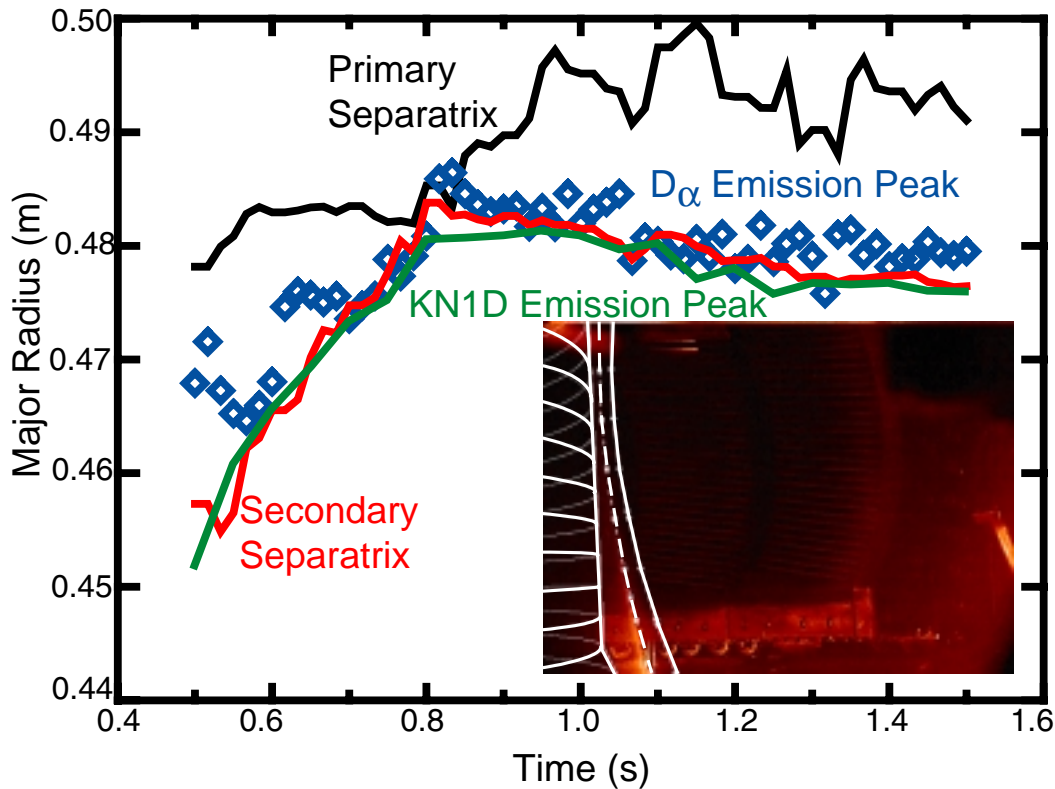


FIG. 15. The location of the radial peak in  $D_\alpha$  emission (and thus that of the most intense ionization) is shown, by the blue diamonds, as a function of time as the magnetic topology is changed from lower single null ( $t < 0.7$  s) through double null (around  $t = 0.8$  s) to upper single null ( $t > 0.9$  s). The high-field side midplane locations of the primary and secondary separatrices, as derived using EFIT, are shown by the black and red curves, respectively. Modeling results from the KN1D code (green curve) show excellent agreement with the experiment. The inset photo shows an image of the  $D_\alpha$  emission at one time in the discharge. The dashed curve shows the location of the secondary separatrix, while the nearly parallel solid curve is the primary separatrix.

## 5. Future Program



FIG. 16. Picture of 12 klystrons (4.6 GHz, 0.25 MW/unit) installed in the C-Mod experimental cell.

Our future program plans to take advantage of the long pulse length possible on C-Mod ( $\sim 5$  seconds) at moderately reduced field (5 T) relative to the plasma current profile evolution time (which is a fraction of  $L/R \approx 3$  s at  $T_{e0} = 5$  keV). This allows C-Mod plasma currents to be fully relaxed during Advanced Tokamak, high confinement, high bootstrap-fraction ( $\geq 70\%$ ) operation [28]. A Lower Hybrid system is being added to provide off-axis current drive. The 4.6 GHz klystrons

from Alcator C have been installed (Fig. 16), and a new multi-waveguide launcher is being constructed at PPPL. The launcher is scheduled for installation in the spring of 2003. We have already demonstrated plasma operation for 3 second pulses, limited only by the flux swing in the Ohmic transformer.

In preparation for the experiments, modeling of startup scenarios is being carried out. Dynamic simulations are performed with the TRANSP code using the LSC lower hybrid module and the NCLASS neoclassical module. Simulations combine enhanced confinement from reversed shear, and high bootstrap fraction from peaked density profiles. Reverse shear is initially formed using a fast current ramp and 3 MW of hydrogen minority ICRF heating. Lower hybrid current drive (LHCD) at the 2 MW level is then applied, 0.15 seconds into the discharge, to maintain the reverse shear and replace the ohmic current.

Profiles consistent with those seen in ITB discharges are specified for the density as well as the ion and electron thermal diffusivity. The density barrier is located at  $r/a = 0.5$ , having a width of 5 cm, with  $n_{e0} = 3 \times 10^{20} \text{ m}^{-3}$  and  $n_{e\text{edge}} = 0.8 \times 10^{20} \text{ m}^{-3}$ . The ion and electron thermal diffusivities are taken to be identical, and equal to  $0.2 \text{ m}^2/\text{s}$  inside the barrier, increasing to  $1.0 \text{ m}^2/\text{s}$  through the 5 cm barrier width, and maintained at this value to the edge of the plasma.

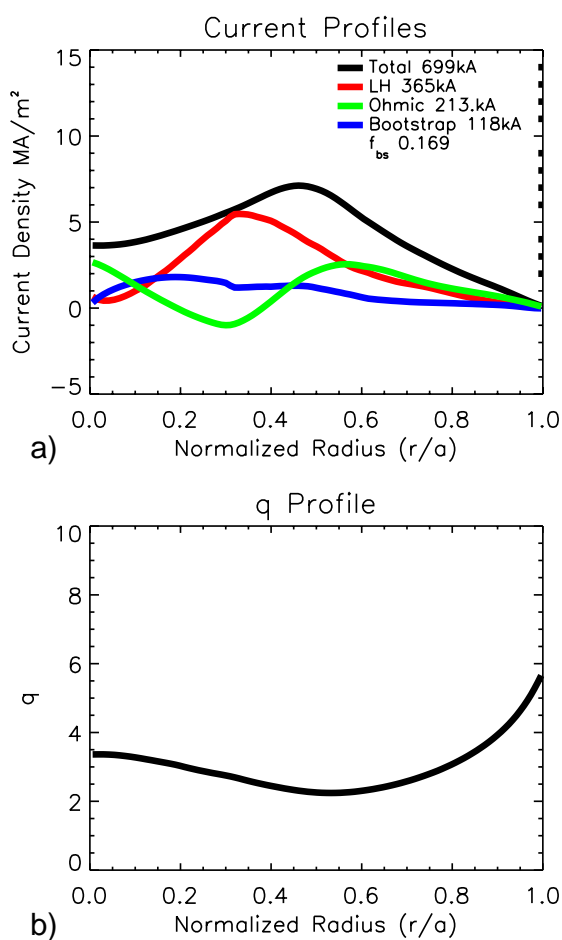


FIG 17. TRANSP-LSC simulation showing inductive response to LHCD at  $t = 0.151 \text{ s}$ : (a) current density profiles; (b)  $q$  profile.

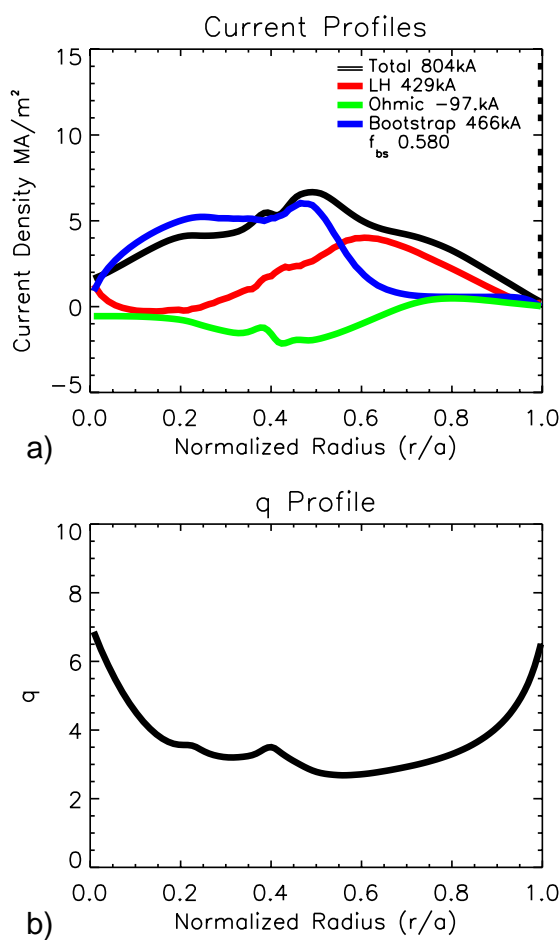


FIG 18. TRANSP-LSC simulation showing high bootstrap fraction, Ohmic recharge, and current hole at  $t = 1.0 \text{ s}$ : (a) Current density profiles; (b)  $q$  profile.

Figures 17 and 18 show the current and  $q$  profiles for two times: just after the LHCD begins and at the end of the simulation. Figure 17(a) shows the inductive response (green trace) just after the start of LHCD. The corresponding  $q$  profile is shown in Fig. 17(b) and exhibits clear shear reversal, with  $q(0) \sim 3.4$  and  $q_{\min} \sim 2.2$  near  $r/a = 0.5$ . The last time slice of the run is shown in Fig. 18. The currents are still evolving and are forming a current hole at the axis. The bootstrap fraction is 58%, and causes the system to be overdriven (at fixed total current), giving the negative ohmic current. The total LHCD power required to achieve this scenario experimentally can be expected to be closer to 3 MW, since LSC does not include particle trapping or the effects of the negative component of the LH power spectrum that will be present.

#### Acknowledgement

This work is supported by the US Department of Energy.

#### References

- 
- 1 HUTCHINSON, I.H., et al., Phys. Plasmas **1** (1994) 1511
  - 2 TAKASE, Y. et al., Phys. Plasmas **4** (1997) 1647
  - 3 WUKITCH, S.J., et al., Phys. Plasmas **9** (2002) 2149
  - 4 RICE, J.E., et al., Nuclear Fusion **42** (2002) 510
  - 5 RICE, J.E., et al., Nuclear Fusion **41** (2001) 277
  - 6 RICE, J.E., et al., Nuclear-Fusion. **38** (1998) 75
  - 7 HUTCHINSON, I.H., et al., Phys. Rev. Lett. **84** (2000) 3330
  - 8 STEK, P., Ph.D. Thesis, Dept of Physics, Mass. Inst. Tech. (1997)  
[http://www.psfc.mit.edu/library/97rr/97rr005/97rr005\\_full.pdf](http://www.psfc.mit.edu/library/97rr/97rr005/97rr005_full.pdf)
  - 9 GREENWALD, M., et al., Plasma Phys. Control. Fusion **42** (2000) A263
  - 10 MAZURENKO, A., et al., Phys. Rev. Lett. (Oct. 2002) in press
  - 11 XU, X.Q., Plasma Science and Technology **3** (2001) 959
  - 12 MOSSESIAN, D.A., et al., Plasma Phys. Control. Fusion **44** (2002) 423
  - 13 MILLER, R.L., et al., Phys. Plasma **4** (1997) 1062
  - 14 SNYDER, P.B., et al., Phys. Plasmas **9** (2002) 2037
  - 15 WILSON, H.R., et al., Phys. Plasmas **9** (2002) 1277
  - 16 DEGTYAREV, L., et al., Comput. Phys. Comm. **103** (1997) 10
  - 17 FERRON J.R. et al., Phys. Plasmas **7** (2000) 1976
  - 18 TAKASE, Y., et al., AIP Conference Proceedings **403** (1997) 33
  - 19 CRADDOCK, G.G., et al., Phys. Plasmas **1** (1994) 1944
  - 20 NELSON-MELBY, E., Ph.D. Thesis, Dept of Physics, Mass. Inst. Tech. (2001)  
[http://www.psfc.mit.edu/library/01rr/01RR006/01RR006\\_full.pdf](http://www.psfc.mit.edu/library/01rr/01RR006/01RR006_full.pdf)
  - 21 PERKINS, F.W., Nuclear Fusion **17** (1977) 1197
  - 22 NELSON-MELBY, E., et al., Submitted to Phys. Rev. Lett. (2002)
  - 23 BRAMBILLA, M., Plasma Phys. Control. Fusion **41** (1999) 1
  - 24 ZWEBEN, S., et al., Phys. Plasmas **9** (2002) 1981
  - 25 GREENWALD, M., et al., Nuclear Fusion **28** (1988) 2199
  - 26 LABOMBARD, B., et al., Phys. Plasmas **8** (2001) 2107
  - 27 LABOMBARD, B., MIT PSFC Technical Report PSFC-RR-01-3 (2001)  
[http://www.psfc.mit.edu/library/01RR/01RR003/01RR003\\_full.pdf](http://www.psfc.mit.edu/library/01RR/01RR003/01RR003_full.pdf)
  - 28 BONOLI, P.T., et al., Plasma Phys. Control. Fusion **39** (1997) 223